

VAMOS: a SmallSat mission concept for remote sensing of Venusian seismic activity from orbit

Brian M. Sutin^{*a}, James Cutts^a, Alan M. Didion^a, Mélanie Drilleau^b, Matthew Grawe^c, Jörn Helbert^d, Ashley Karp^a, Balthasar Kenda^b, Attila Komjathy^a, Siddharth Krishnamoorthy^a, Gregory Lantoine^a, Philippe Lognonné^b, Jonathan J. Makela^c, Barry Nakazono^a, Mayer Rud^a, Mark Wallace^a
^aJet Propulsion Laboratory, California Institute of Technology, 4800 Oak Grove Drive, Pasadena, CA 91109-8099; ^bInstitut de Physique du Globe de Paris, Sorbonne Paris Cité, 35 rue Hélène Brion, 75013, France; ^cUniversity of Illinois at Urbana-Champaign Urbana, IL 61801; German Aerospace Center, Institute for Planetary Research | PF-XP, Rutherfordstrasse 2 12489 Berlin, Germany

ABSTRACT

The apparent youthfulness of Venus' surface features, given a lack of plate tectonics, is very intriguing; however, long-duration seismic observations are essentially impossible given the inhospitable surface of Venus. The Venus Airglow Measurements and Orbiter for Seismicity (VAMOS) mission concept uses the fact that the dense Venusian atmosphere conducts seismic vibrations from the surface to the airglow layer of the ionosphere, as observed on Earth. Similarly, atmospheric gravity waves have been observed by the European Venus Express's Visible and Infrared Thermal Imaging Spectrometer (VIRTIS) instrument. Such observations would enable VAMOS to determine the crustal structure and ionospheric variability of Venus without approaching the surface or atmosphere. Equipped with an instrument of modest size and mass, the baseline VAMOS spacecraft is designed to fit within an ESPA Grande form factor and travel to Venus predominantly under its own power. Trade studies have been conducted to determine mission architecture robustness to launch and rideshare opportunities. The VAMOS mission concept was studied at JPL as part of the NASA Planetary Science Deep Space SmallSat Studies (PSDS3) program, which has not only produced a viable and exciting mission concept for a Venus SmallSat, but has also examined many issues facing the development of SmallSats for planetary exploration, such as SmallSat solar electric propulsion, autonomy, telecommunications, and resource management that can be applied to various inner solar system mission architectures.

Keywords: Venus, Airglow, Ionosphere, Atmosphere, Infrared, Remote Sensing, SmallSat, SEP, seismology

1. INTRODUCTION

Observations which can reveal characteristics of Venus's internal structure, crustal dynamics, and level of seismic activity are highly desirable, yet very hard to obtain via surface investigations. Surface missions utilizing a seismometer could take direct measurements of seismic phenomena, but suffer incredibly harsh conditions to do so, drastically limiting their lifetimes and driving up costs. By exploiting the medium of airglow, an ionospheric phenomenon which betrays pressure waves in the atmosphere (the strongest of which happens to belong to Venus), orbital infrared measurements can replace risky and difficult surface investigations. A second advantage of orbital measurements is that these observations replace the need for a seismic network, since each pixel observed corresponds to a seismic record.

The Venus Atmospheric Measurements and Orbiter for Seismicity (VAMOS) concept has the potential to collect invaluable and classically difficult to obtain data from orbit within small mass, volume, and cost allocations. The use of a relatively simple instrument and compact spacecraft enables the delivery of VAMOS to Venusian orbit via a variety of launch date-flexible and cost-effective means. The orbit and launch of the VAMOS concept are designed to be flexible and make use of Venus-bound as well as popular commercial geostationary transfer orbit (GTO) rideshare opportunities, while the spacecraft fits within the EELV Secondary Payload Adapter (ESPA Grande) mass and volume allocations.

^{*}brian.m.sutin@jpl.nasa.gov; phone 1 818 354-2227; fax 1 818 393-3290; <https://www.jpl.nasa.gov>

VAMOS can be readily paired with other concepts in a synergistic manner to increase overall science return, serving to revive interest in and reveal the secrets of Earth's twin planet.

The difficulties faced in the development of the VAMOS concept are common to the majority of investigations which rely on SmallSat technology, such as small solar electric propulsion (SEP), SmallSat component lifetime and technology readiness level (TRL), and on-board processing and autonomy. The resulting lessons learned will benefit large space investigations and the growing SmallSat class alike.

2. SCIENCE INVESTIGATION

Because of its unique orbit, allowing a continuous monitoring of Venus atmosphere, VAMOS is the ideal platform for atmospheric wave propagation monitoring, as well as tracking other ionospheric and atmospheric time-evolving phenomena. Our proposed science investigations focus on the feasibility of detection of seismically coupled acoustic waves, targeting large amplitude surface waves generated by Venus quakes. The measurement of phase and group velocity of the waves would provide both global and regional measurements of the crustal thickness, while the occurrence and intensity would be related to Venus seismicity.

In our investigations, we modeled both the 1.27 μm nightglow and the dayside 4.28 μm non-local thermodynamics equilibrium (non-LTE) signals associated with the waves, and results show that the detection threshold for the VAMOS imager expected performances is Ms 6 (Surface Wave Magnitude Scale) for 1.27 μm and Ms 5 for 4.28 μm . With the expected level of seismicity of Venus (~25 times less than Earth) and about half these quakes occurring on the night-side of VAMOS, this might provide us about 2 and 25 detections per year respectively, including 5 or more with wave detection strong enough to allow regional studies on crustal thickness including investigating Venus lowland, high lands and Tesserae. Additional science goals that are associated with the propagation monitoring of atmospheric gravity waves and plasma disturbances would complement the threshold science goals of the VAMOS concept. They would also constrain the atmospheric gravity waves generated by the interaction of the atmosphere with Venus topography and together with the specific seismic goal, would provide a comprehensive and revolutionary view of the coupling processes between a planetary interior and its atmosphere.

2.1 Investigation Background, Goals, and Objectives

2.2.1 Atmospheric Seismic Coupling

VAMOS seismic goals and objectives are based on the capability to detect at high altitude seismic Rayleigh waves caused by Venus quakes. Such high-altitude atmospheric and ionospheric disturbances which are associated with acoustic waves generated by the Rayleigh surface waves have been routinely observed on Earth in the far field of very large ($M_w > 7$) quakes^{1,2,3} in addition to the near-field of smaller quakes. Calais and Minster⁴ reported observations following the Northridge $M_w=6.7$ (Moment Magnitude Scale) earthquake and Kelley *et al*⁵ for an even smaller quake with $M_w=5.9$. These observations have furthermore led to the determination of the phase and group velocity of surface waves, with a resolution enabling the measurement of lateral variations in the surface wave velocity¹ or surface wave scattering associated with 3D structure².

VAMOS would benefit from a much stronger seismic coupling of Rayleigh waves in the Venus atmosphere compared to the case of Earth, due to the high density and pressure at the interface between the Venus solid planet and its atmosphere. This is illustrated in Figure 2-1, which compares the coupling strength between Earth, Venus and Mars. This demonstrates that Venus is the only terrestrial planet where such increased coupling would compensate the expected smaller seismic activity of the planet as compared to Earth. The atmospheric seismic wave coupling on Venus has been extensively studied by Garcia *et al*³, Lognonné and Johnson^{6,7}, and Lognonné *et al*⁸.

2.2.2 Airglows Seismic Emission

Due to the dynamical coupling between the solid planet and the atmosphere, the waves generated by quakes propagate and can be detected in the atmosphere itself^{3,6,7}. This has been demonstrated on Earth using various techniques with different observations and physical principles. For example, the excitation of the visible 630 nm (red) airglow and GPS total electron content (TEC) perturbations resulting from the propagation of tsunami waves and Rayleigh waves was detected after several earthquakes over the past five years. In Figure 2-2, we show the airglow tsunami signature, resulting from the Sept 18, 2015, Chile earthquake and tsunami⁹. These images are taken using a wide-angle camera system located at the top of

the Haleakala Volcano on Maui, Hawaii. Similar imaging was performed for the 2011 Tohoku-Oki and 2015 Haida Gwaii events¹⁰.

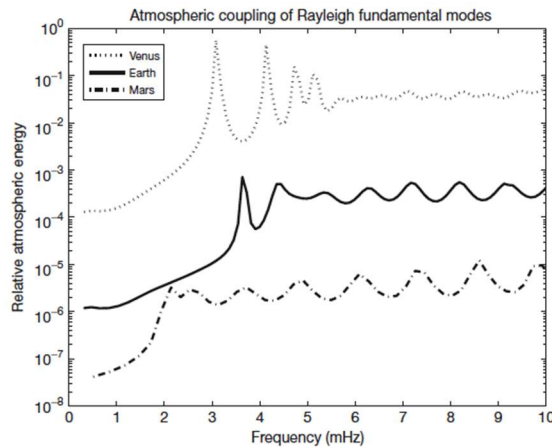


Figure 2-1. Fraction of the surface-wave energy in the Venus, Earth, and Mars atmospheres for Rayleigh surface waves. Only the first peaks are due to atmospheric resonances. Note that the amplitudes on Mars and Earth are comparable at low frequency (2–3 mHz) due to differences in the atmospheric resonance frequency.

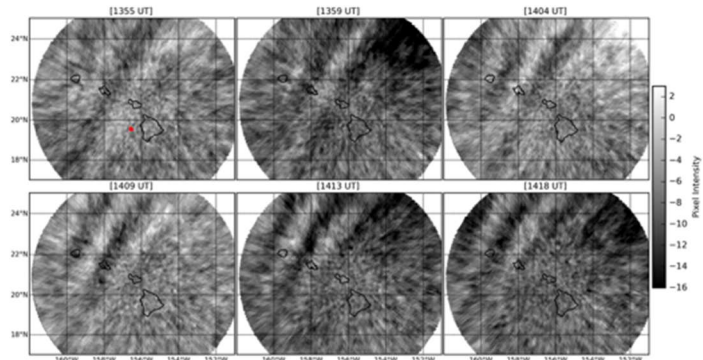


Figure 2-2. Tsunami-generated airglow perturbations near Hawaii generated by the Sept 18, 2015 earthquake near Chile⁹.

2.2.2.1 1.27 μm Airglow

Seismic waves generate airglow emissions at 1.27 μm and 4.28 μm through different physics-based processes. The 1.27 μm nightglow disturbances are associated with seismic waves via transport of the glowing media as caused by the very long radiative lifetime of the 1.27 μm nightglow emissions ($\sim 4,460$ sec). The altitude of the airglow on Venus is maximum at an altitude of about 100 km. The strength of the emission is about 0.5 mega-Rayleigh (MR) on average, with large fluctuations amounting up to 3 MR.

Lognonné *et al*⁸ shows that the 1.27 μm airglow signal is related to the mean of the Volume Emission Rate (VER) flux in the emitting region. We find that for small quakes, the vertically propagating waves appear to show oscillations with mean value close to zero. However, the large VER gradient, shown in Figure 2-3, is critical in generating the asymmetry of the incoming waves, which will generate non-zero VER flux after integration. Figure 2-3 illustrates this phenomenon using a Gaussian wave, which is similar in shape to the waves generated by techniques using synthetics. We note that the VER maximum does not correspond to the maximum of the observed flux value, due to the amplification factor of the wave with altitude dependence, which is inversely proportional to the squared root of density times sound speed. This simple model allows us to get a better understanding and an estimate of the filtering effect of airglow layer for waves with a given velocity amplitude as waves propagate upwards. This suggests that the airglow amplitude after integration along the line-of-sight (assuming nadir direction) seems larger when the wave arrives at the lower boundary of airglow layer compared to the wave exiting the airglow layer due to the steeper airglow VER gradient below the maximum VER (see Figure 2-3). As an example, for a 50-sec wave with a vertical velocity amplitude of 0.04 m/s at 100 km altitude (corresponding to an amplitude generated by an Ms ~ 6.5 quake at 10° of epicentral distance), our simulation finds intensities of about 0.02% of the background VER resulting in about a 400-Rayleigh signature compared to about 2 mega-Rayleigh background intensity. This, however, decreases to only 20 Rayleigh for 10 second waves since the airglow layer operates as an analogue filter with about 20 dB attenuation per decade. However, our simple modeling approach depends strongly on the shape of the waves and so more precise modeling with simulated waveforms is necessary and is developed in the Section 2.2. This approach however illustrates the filtering effects we can encounter on Venus.

2.2.2.2 4.28 μm Airglow

The 4.28 μm seismic airglow signal is primarily related to temperature variations that are associated with the adiabatic temperature changes generated by the propagating waves but also, in hot conditions, to the large temperature variations of the background which might be transported by the seismic wind. As 4.28 μm airglow occurs at altitude ranging from 115–135 km (Figure 2-4), the seismic waves will get amplified compared to those of the 1.27 μm airglow by a factor of about 16 for altitudes of 115 km and by a second amplification of about 8 between 115–135 km).

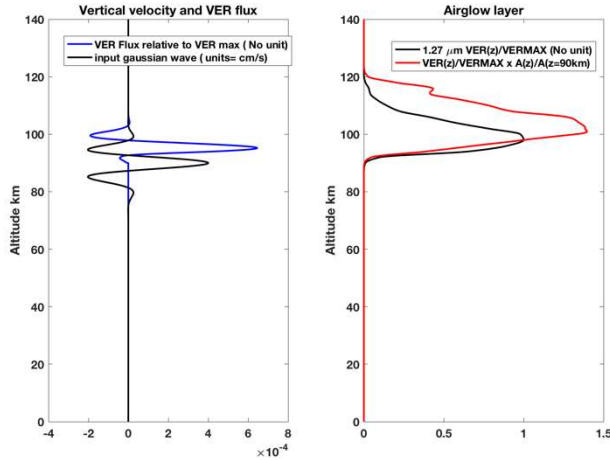


Figure 2-3. Simplified emission model for a Gaussian wave travelling upward with a maximum of 0.04 m/s at 90 km altitude. The wave, without height amplification, is shown on the left, with amplitude reduced by 100. The right panel provides the VER scaled to its maximum (in black) and the product of the scaled product of VER by the amplification (A) ratio relative to 90km altitude (in red). Blue line on the left is the corresponding relative VER flux scaled to VER maximum, which encompasses both the altitude amplification and the VER profile.

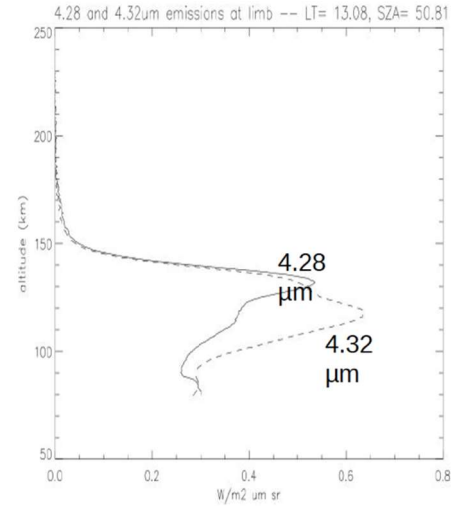


Figure 2-4. Altitude of the 4.28 μm (and 4.32 μm) airglow VER as a function of limb emission¹¹.

The variations of CO_2 non-LTE emissions, observed from nadir with 30 nm spectral resolution, were then simulated by computing the energy levels of CO_2 states and their transitions in a radiative transfer code^{12,13}. In order to obtain the sensitivity of these emissions to the atmospheric perturbations induced by acoustic waves, these computations were performed using an unperturbed model versus a model in which only the temperature perturbation was considered. The difference between the two emission spectra is presented in Figure 2-5. The maximum emission perturbation is observed at 4.28 μm wavelength for perturbations in the 120–140 km altitude range and presents a relative amplitude of 5%. This sensitivity of 1%/K is consistently observed, at this wavelength and in this altitude range, for various atmospheric models tested (not shown). This result is also consistent with previous computations performed with the limb geometry¹⁴.

Throughout this paper, surface wave magnitude (M_s) will be assumed to be equal to the moment magnitude (M_w), the later related to seismic moment by $M_s = 2/3 (\log_{10}(M_0) - 9.1)$, where M_0 is the seismic moment in Nm). In both cases, the vertical integration results in filtering the seismic signals and serves as 2nd order low pass filter, which will limit the wave detection to the long period (larger than 10–20 sec) waves.

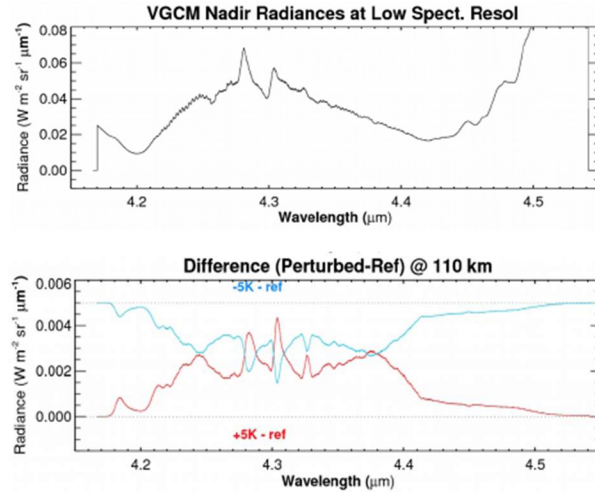


Figure 2-5. Top panel indicates typical nadir radiance. Bottom panel displays radiance perturbation for a 5°C temperature perturbation at 110 km altitude.

2.2 Modeling of Airglow Signatures on Venus

Figures 2-6 shows simulated measurements for 1.27 μm . The 4.28 μm band is similar. In the simulations, the pixel data have been stacked on 5×5 pixels in space and 5 consecutive time epochs corresponding to post-stack resolutions of 25 km and 10 seconds. The Venus quake source is assumed to be isotropic, while real quakes have double coupled source, resulting in degree two radiation patterns. This however is not expected to change the amplitudes in a significant way. For the 1.27 μm , the background is assumed to be constant over time, but with features corresponding to the one observed on VEX. All radiances are computed for nadir direction and off nadir effects would be computed in future developments. At 60° from nadir the background radiance would be increased by 2, with an effective pixel apparent size of 10 km which remains significantly smaller than half a wavelength of a 20 second surface wave (70 seconds). Off-nadir corrections are therefore expected to be small in the science FOV ($\pm 60^\circ$ around the planet to satellite nadir) and would be managed in subsequent steps. For all figures below, we also computed the stacked signals as function of epicentral distance by stacking all pixels for a given epicentral distance. For an isotropic source, this can be done directly, while for a double couple, this would need to be done with azimuth corrections in order to integrate the radiation polarity in the stack. This was performed on the simulated data (affected by shot noise) and on the noise-free synthetics, estimating the expected data quality data for 1D analysis, such as the determination of the average velocity of surface waves.

These simulations indicate that the shot noise associated with the background is the most significant source of noise compared to the signal strength. For 1.27 μm , about 30,000 and 43,000 photons for an $f/4$ and $f/3$ optical design respectively, are hitting each pixel for a 2 second integration time. The associated shot noise will have an RMS of 0.57% and 0.48% of the background, respectively and are thus larger than the expected signal. The stack on 25×5 pixels reduces the relative shot noise by a factor of about 11, resulting in a peak-to-zero shot noise of approximately 60 photons, which comparable to the amplitude of the signal for a M_s 6.5 quake as shown in our modeling (Figure 2-6a) using distances of about 30° – 40° as shown in the images. Stacks with respect to epicentral distances are, therefore, required to achieve a favorable SNR for the waveforms. Note the comparison of the stacked signals as epicentral distance and of the noise-free signal, in Figures 2-6. However, the high shot noise prevents good detection chances below M_s 6 and a detection threshold is likely of about M_s 6 for distances smaller than 20° . Even if the 1.27 μm provides important monitoring capabilities on the night side, this window alone is not able to meet the science goal requirements in terms of detection threshold.

The 4.28 μm airglow emission is much brighter and the typical background is expected to be 16 times in terms of photon number, which will reduce the shot noise by a factor of about 4. In addition, as shown by the comparison of Figures 2-4 and 2-5, the signal amplitudes are expected to be larger. This is mostly related to the difference of altitudes, as the 1.27 μm senses at about 100 km, while the peak of 4.28 μm is at 135 km. At these altitudes, both the temperature (ranging from 200–260 Kelvin depending on the model) and the molecular mass of CO_2 result in a height scale of about 5 km, leading

to amplifications of the wave by 4.5 between 100 km and 115 km and by an additional factor of 8 between 115 and 135 km.

Assuming a temperature sensitivity of 1% of the background per Kelvin, much improved SNR observations will therefore be expected. Signals can be observed for surface waves up to 20° of epicentral distance and such magnitude is likely to be at the detection threshold for baseline goal.

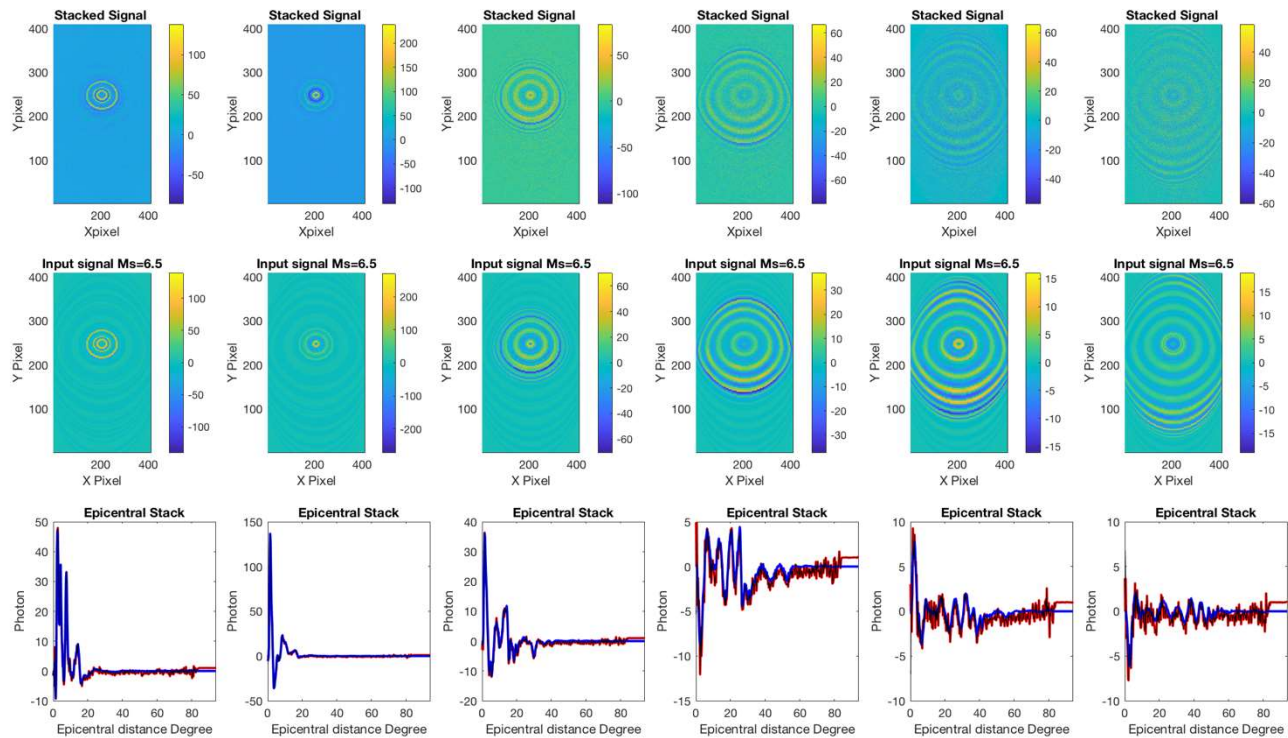


Figure 2-6. Results for Ms 6.5 and $1.27 \mu\text{m}$. Snapshots are taken at every 5 minutes, showing the propagation of waves. Stacks are computed using 25 pixels encompassing an area of $25 \text{ km} \times 25 \text{ km}$ and time period of 10 sec. Units are photon numbers at the pixel level. The shot noise in the major contributor of the stacked signal noise. The figures at the bottom are comparing the noise free signal (in blue) with the signal obtained by a further stack of the pixels with respect to epicentral distance. A much better fit and SNR is then achieved, enabling good waveform inversion perspectives.

3. VAMOS INSTRUMENT

The VAMOS instrument is a relatively simple infrared telescope designed to continuously stare at Venus, waiting for evidence of seismic events. The design features optics that facilitate observation of a large fraction of the planet at once from the nominal orbit. The design features novel algorithms running on a dedicated processor to detect and record events from a real-time stream of incoming data.

3.1 Instrumentation

The instrument images the disk of Venus at two wavelengths: the $1.27 \mu\text{m}$ airglow band for non-sunlit (night-side) regions, and the $4.28 \mu\text{m}$ band for the sunlit (day-side) regions. The resolution requirement is to detect waves in the airglow region with a wavelength of 70 km over a significant portion of the visible disk, so the spatial sampling at nadir must be near 5 km/pixel, taking into account foreshortening from the planet and the Nyquist criterion. The minimum field of view required for seismic science is a circle centered on the nadir point with a radius of 65° longitude, while for gravity (buoyancy) waves, a much larger field of view is desired. The current baseline field of view is a square centered on nadir with the sides at 75° longitude. The instrument design uses two Teledyne H2RG detectors with two Teledyne SIDECAR readout ASICs¹⁵. In order to save on cost, both detectors are likely to be $5.3 \mu\text{m}$ cutoff, and both kept near 80–85 K in order to reduce dark noise. The two SIDECAR ASICs are controlled by a radiation-hard CubeSat-style electronics board set,

consisting of a LEON3 processor and a Microsemi FPGA. The electronics use about 7 W, with contingency. A computer residing in the warm compartment of the S/C, runs the event detection algorithm.

3.1.1 Optical Design

An optical design trade between reflective and refractive designs settled on a refractive design as the most appropriate. Here we summarize the plethora of reflective designs and describe the main reasons for choosing the refractive concept instead. Since the $1.27\text{ }\mu\text{m}$ channel observes the unlit side of Venus, a major design consideration is stray light from the Sun being very near the field of view.

Initial designs were all $f/4$. The field of view to see most of Venus from the 45,000 km orbit is about 15.6° , leading to a focal length of 135 mm and an aperture of 34 mm. A projected pixel on the ground is turned out to be 5160 km. Filters for each band are as narrow as can be tolerated by the $f/4$ beam, so on the order of 12 nm ($1.27\text{ }\mu\text{m}$) and 30 nm ($4.28\text{ }\mu\text{m}$) bandwidth.

The first design considered was an all-reflective unobstructed three-mirror anastigmat (TMA). See Figure 3-1d. Since this all-mirror design has no wavelength dependence and can be made all aluminum, the design has no temperature dependence, and the two detectors can share one set of optics by using a beamsplitter. The drawback of the all-reflective design is that the TMA has no internal field stop, so the only method of controlling stray light from the sun is to use an external baffle. As the field of view of the instrument is very large (more than 15°), the baffle must be almost as long as the spacecraft and is only able to control stray light when the Sun is more than 10° from Venus. This design would therefore require a steep orbital tilt with respect to the ecliptic in order to take data when a significant fraction of the non-sunlit side of Venus is being viewed.

Several other reflective designs were also considered, namely a Cassegrain telescope with a mirror collimator, as well as a lengthened TMA with an internal field stop. See Figure 3-1 (a,b,c) for the different configurations. All of these designs were highly non-telecentric (unacceptable because of the narrow filter band-passes) and would require correction with wavelength-dependent prism field flatteners.

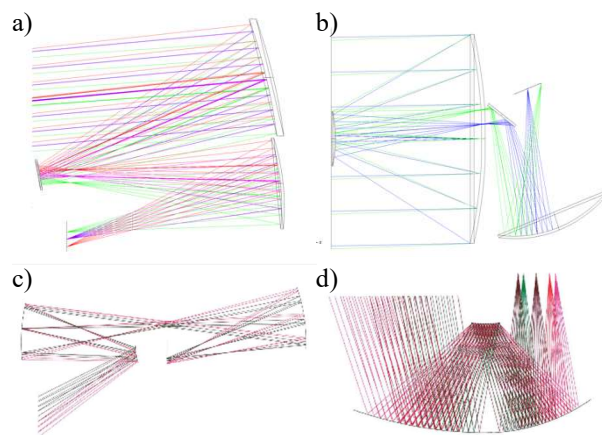


Figure 3-1. Plethora of rejected reflective designs: (a) TMA with accessible field stop (b) Cassegrain with re-imager (c) unobstructed telescope and re-imager (d) compact TMA.

The final refractive concept (Figure 3-2), similar to that used on VIRTIS/VEM¹⁶, has an internal field stop, and is highly capable of excluding stray sunlight. Refractive designs can suffer from thermal issues, so the refractive design may require careful thermal control of the lenses. Because of the internal field stop, the optimal untilted orbit, which can have the Sun directly behind Venus, is allowed. Further work on the optical design would be to shorten the overall length, remove extra lens elements, athermalize the design, and use a wedged plate beamsplitter rather than a beamsplitter cube. Another possibility, if more bands are desired, is to switch to a single detector and a filter wheel.

Since the refractive design is axially symmetric and the total length of 650 mm would fit comfortably in a SmallSat, the mechanical design is relatively straightforward. Space exists between the lens groups for fold mirrors, if required. The entire instrument is on the order of 5 kg with contingency.

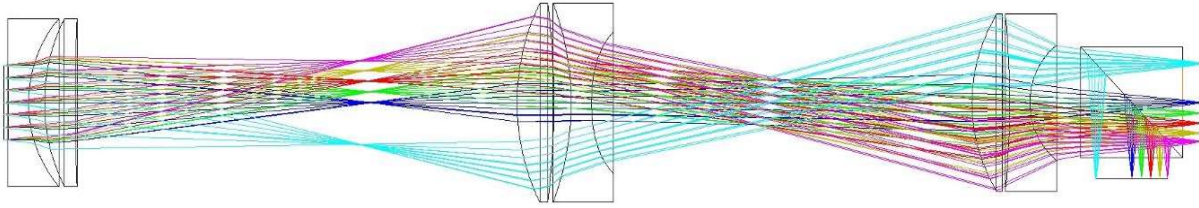


Figure 3-2. Baseline concept refractive design (aperture to the left, detectors behind a beamsplitter cube on the right). Materials are, in order, (CaF₂-Cleartran), (ZnSe-CaF₂), (ZnSe-CaF₂), and a CaF₂ beamsplitter cube. The field stop between the first two doublet lenses and the Lyot (or pupil) stop between the next two doublet lenses are evident.

3.1.2 Thermal Design

The thermal design consists of a two-stage cryo-radiator (Figure 4-4). The cryo-radiator is placed on the opposite side of the S/C from the solar panel, so that the face of the cryo-radiator is never illuminated by the Sun. The first stage cools the SIDECAR ASICs to 150 K, while the second stage cools the detectors to 80 K. Since the instrument is shot-noise limited (see Section 3.2), the dark current can be much higher than for a typical astronomy or deep-space mission. A detector temperature as high as 85 K would likely be acceptable. The warm electronics are cooled with a separate radiator shared with the S/C.

3.2 Instrument Performance Modeling

The refractive optical design has a spot FWHM of less than a pixel, making the design diffraction limited at 4.28 μm . See Figure 3-3.

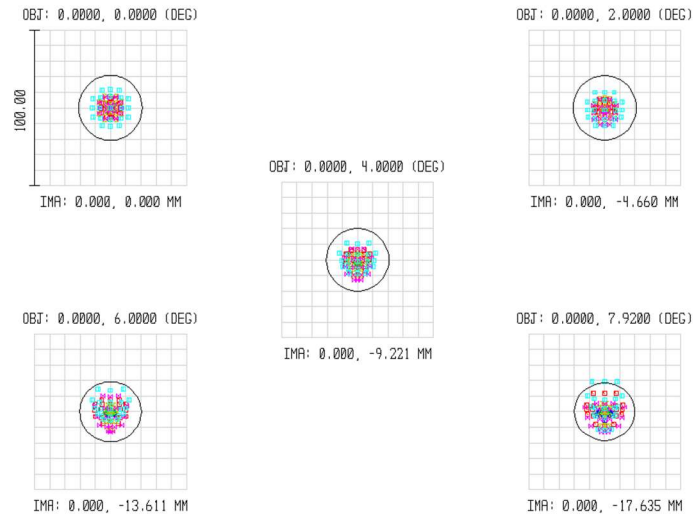


Figure 3-3. F/4 refractive camera performance is diffraction limited.

In the time domain, waves are expected from seismic events at frequencies up to 0.2 Hz, or a period of 5 seconds. In order to prevent these waves from aliasing into lower frequencies, VAMOS samples at 0.4 Hz (2.5 seconds), and then uses a symmetric 11-point FIR filter, as shown in Figure 3-4. The result is then sampled at 0.2 Hz to generate an anti-aliased image every 5 seconds.

The signal-to-noise ratio (SNR) achieved by VAMOS is driven by shot (Poisson) noise from the high airglow background. The full well capacity of the H2RG detector is around 65,000 electrons, so a half-full-well image frame has an SNR per pixel of $\sim 0.5\%$. The expected wave signal is also on the order of 0.5% of the airglow, so the SNR of a single frame is ~ 1 . Compared to the airglow shot noise, contributions from dark current, read noise, and solar background are all negligible. The shortest time that the detector can be read out in slow mode (where the read noise is genuinely negligible) is 0.27 seconds.

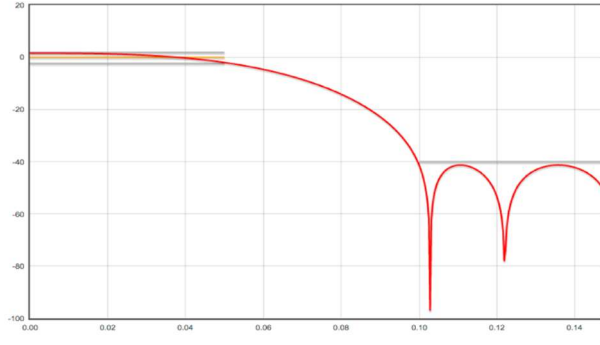


Figure 3-4. 11-pole symmetric anti-aliasing filter frequency response.

For the 4.28- μm band, a neutral density filter with approximately 40% throughput is required to prevent saturation due to the airglow. For this band, the detector is then read out with an exposure time of 0.27 seconds, and the sub-frames are combined using up-ramp sampling to produce the 2.5-second frame rate. The final noise per frame per pixel is ~ 3 . An alternative to a neutral density filter is to use high-speed readout of the detector, at the cost of extra readout noise. The two approaches are likely to result in similar SNR.

For the 1.27- μm band, the detector just reaches half-well with an exposure time of $(2.5-0.27=2.23)$ seconds, and so correlated double sampling (CDS) can be used for readout. The final noise is estimated to be ~ 1 per pixel per frame.

3.3 Detection Algorithms

An onboard software algorithm is used to detect seismic waves, so that an entire seismic wave sequence can be detected, compressed, and downloaded. Although gravity waves are also seen in the airglow, gravity waves have a different timescale and wavelength and are easy to discriminate from seismic waves. Grawe and Makela⁹ developed an automated technique that requires little human interaction in processing airglow wave measurements. The technique has potential in enabling large-scale statistical studies as well as real-time monitoring of seismic events. The original technique was employed for use with ground-based imaging systems and utilized a combination of Gabor filtering (commonly used for feature extraction) and periodogram analysis to yield measurements of wavelength, orientation, speed, and period. A modified version of the algorithm has been developed for use in a time-critical setting onboard a moving platform, which is the use-case we explore here. This modified algorithm, as well as its expected performance, is described below. An example of a periodogram is shown in Figure 3-5.

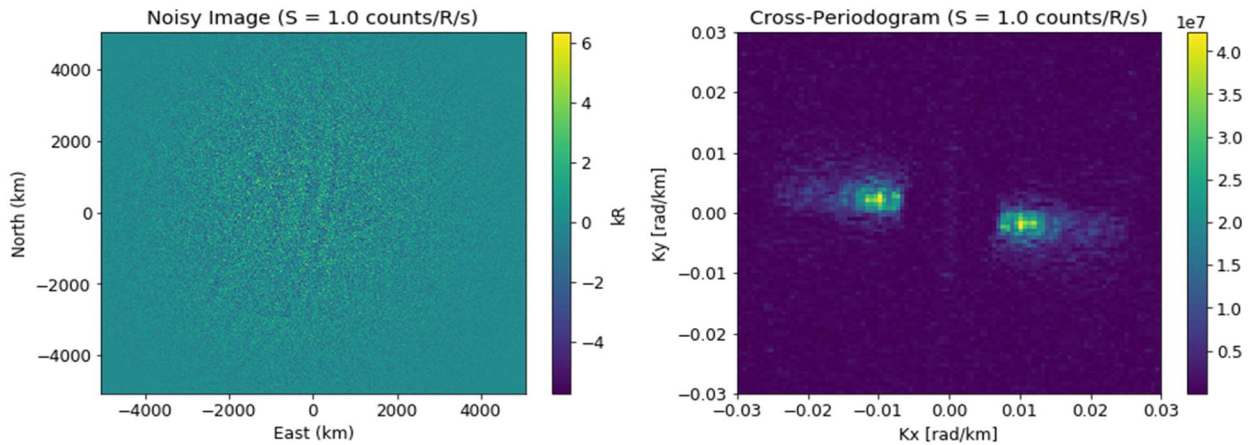


Figure 3-5. (left) Simulated image of raw data; (right) two-frame cross-periodogram demonstrating detection feasibility.

3.3.1 Algorithm Overview

The data processing algorithm is split into *detection mode* and *analysis mode* (Figure 3-6).

Detection mode is designed to run in real-time, continuously providing the result of a wave presence hypothesis test (Figure 3-6f) using a smoothed rolling cross-periodogram (Figures 3-6d,e) on a batch of images. A positive hypothesis indicates the presence of wave activity within a predefined wavelength search space. To run in real-time, detection mode works with a decimated (in space) version of the 0.2 Hz image sequence discussed previously (Figure 3-6a) while still satisfying the Nyquist criterion for the target wave parameters. After decimation, the images are subject to a temporal background removal high-pass filter (Figure 3-6b). This filter is distinct from the 11-point low-pass anti-aliasing filter discussed in Section 3.2. The filtered images are then projected onto a uniformly sampled grid centered at the nadir intersection of the emission layer prior to the cross-periodogram step (Figure 3-6c). When a wave is detected within a set of decimated images, a table of image IDs (each image has a unique ID), and a center k-vector (with the associated energy) are logged. Each set of data (the table and k-vector) is considered as a “block” and the block is added to a queue.

Analysis mode is designed to provide full wave parameter measurements (wavelength, orientation, speed, period) and runs on full-resolution versions of the images in the queued blocks from detection mode (Figure 3-6h). The full-resolution wavelength, orientation, speed, and period are extracted from the phase of the cross-periodogram (Figure 3-6i), timestamped, and transmitted back to Earth along with a spectral mask (Figure 3-6g; an adjustable region of magnitude and phase information centered around the measured k-vector). Any other desired processing too slow for detection mode can also be performed here; analysis mode is not intended to run in real-time (although it may be possible on certain hardware).

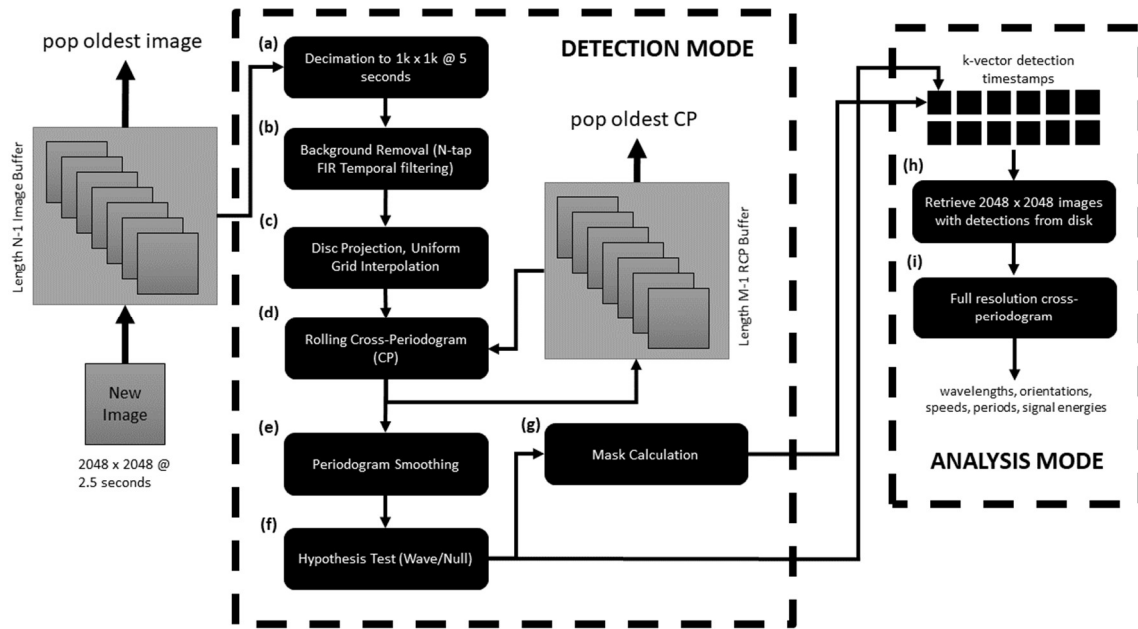


Figure 3-6. Overview of the wave detection and analysis algorithm. Detection mode is designed to run in real time on a decimated version of the image sequence. Analysis mode works with the full resolution data and runs on image blocks triggered by detection mode when switched on.

3.3.2 Benchmarks and Hardware Limitations

In order to assess the ability of detection mode to run in real time as a function of onboard hardware capability, a set of timing benchmarks were run on a 2.4 GHz AMD Opteron 6378 having 4 FLOPs/cycle for several different image sizes. The total flop count inferred from the timings was then used to extrapolate to different hardware capabilities. In the case of a circular orbit, the projection from image coordinates to a uniform grid can be greatly optimized and results in a large speedup relative to an eccentric orbit. It is likely that non-circular orbits are also optimizable (to a lesser degree), however we did not attempt to parameterize this; the results we show are for nearly-circular orbits only.

The benchmarking results suggest that detection mode can run in real-time on a factor-of-two decimation in space and time relative to the baseline 2048×2048 pixel, 2.5 second image sequence (i.e., 1024×1024 at 5 seconds) and report on detected wave activity with at least 90° ($\pm 45^\circ$) longitude coverage relative to nadir. Further performance increases may result by delegating the FFT operations to multiple cores, if available.

3.3.3 Detectability in Noise

Detectability of a Rayleigh wave was assessed by running a 16-trial Monte Carlo simulation of a vertically-integrated, seismically-induced O_2 nightglow intensity perturbation corresponding to a M_w 6.5 earthquake generated using normal modes modeling. The perturbation was added to a vertically-integrated O_2 nightglow background generated using the Venus Thermospheric General Circulation Model (VTGCM)¹⁷ with a peak intensity of ~ 2 MR and realistic detector noise was applied to each trial. The simulated noisy images were then run through detection mode. Background removal was applied using a 7-tap temporal finite impulse response (FIR) filter. The simulations were run for varying degrees of spatial extent (waves with larger spatial envelopes are easier to detect) using a causal Gaussian window centered at the peak of the wave. To mimic the onboard processing, 8 noisy sub-images were generated and spatially co-added. Each sub-image had an independent dark current, read noise, and integration time of 1.7 electrons/sec, 15 electrons/read, and 0.278 seconds, respectively. Figures 3-7a–d show the noiseless perturbations. Figures 3-7e–h show the associated wavelength estimates (run on the noisy, full-background images) as a function of total efficiency (TE; the product of quantum efficiency and optical transmission) using 1–6 pairs (M) in the periodogram smoothing operation. As the TE decreases, a detectability threshold is reached whereby the mean and variance in the wavelength estimate drastically changes. Figures 3-7i–n show the same results but focusing on the breakdown region (except for the 500 km case, which was not detectable).

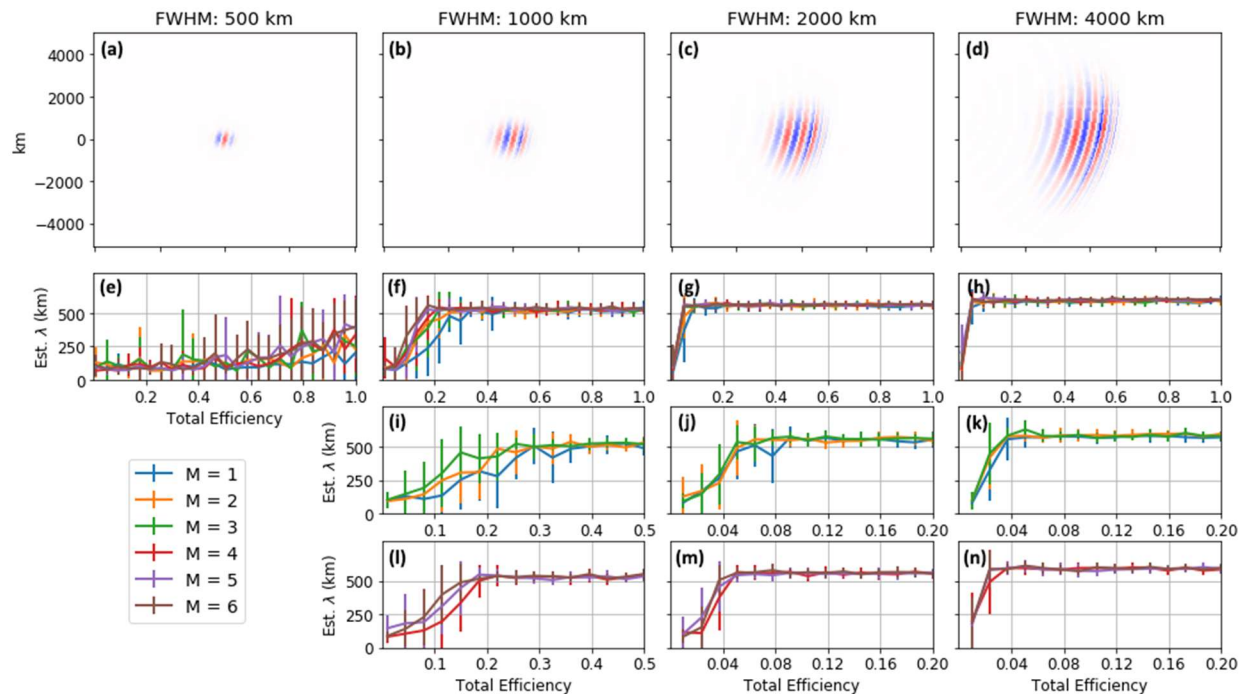


Figure 3-7. Detectability assessment using a 16-trial Monte Carlo simulation of a seismically-induced O_2 nightglow intensity perturbation corresponding to a M_w 6.5 earthquake in shot, dark, and read noise for various spatial extents. The results suggest that detection is possible if the spatial envelope of the wave is ≥ 1000 km and $TE \geq 30\%$. Waves having a larger spatial envelope and/or using more periodogram smoothing leads to a significant further reduction in the threshold TE for detection.

Our results suggest that detection is possible if the spatial envelope of the wave is ≥ 1000 km and $TE \geq 30\%$. Waves having a larger spatial envelope and/or using more periodogram smoothing leads to a significant further reduction in the threshold TE for detection. Using additional smoothing may or may not be valid depending on the temporal variability of the background (in our simulation we did not include this). At the very least, orbital motion of the satellite across the spatially

non-uniform background intensity will likely lead to decreased estimation ability for epicenters occurring on or near the orbital plane and distant from nadir.

3.3.4 S/C Motion Subtraction

Since the airglow brightness is not spatially uniform, the rotation of the view of Venus as the spacecraft orbits affects the detection of waves. The relative motion of the planet and the background airglow, in combination with the imaging frame rate, can cause variations in the background to alias into the data as time-varying signals. This effect can be mitigated in many ways. Resampling the detector pixels with linear interpolation to make the background appear stationary is one method, with the drawback that the point spread function (PSF) contribution from the pixel size varies from frame to frame. Another method is to do small slews of the spacecraft, complicating spacecraft operations. The background could also be analyzed and the variations predicted and subtracted from the data. Each of these methods is simple to emulate and compare.

3.4 Technology Gaps and Key Trades

The instrument as outlined above still has several technology gaps or remaining trade studies that affect the mission, spacecraft, instrument design, and GDS.

3.4.1 Final Data Bandwidth

The fundamental challenge with the VAMOS instrument is limited telecom bandwidth. The instrument itself can generate an anti-aliased $2k \times 2k$ image every 5 seconds, while the telecom can return 20 Mb/orbit when Venus is on the far side of the sun. Consequently, returning raw image data is only realistic for debugging and algorithm tuning. The image data must be reduced on board to a level concise enough to be returned. This leads to two challenges: algorithms that can be trusted to reduce data remotely, and adequate computing power to run said algorithms.

The first step to reduce the amount of data is the implementation of an onboard seismic event detection algorithm (as described in Section 3.3). Although very computation intensive, the detection algorithm prevents sending back uninteresting event-free data.

3.4.1.1 Compute Hardware Trade

The complex onboard software required for the event detection algorithm exceeds the capability of the small FPGA and processor boards used to run the detectors and control the observations. A second computer would be required, residing in the warm compartment of the S/C, to run this algorithm. It is not clear what hardware is optimal for this computer, although preliminary benchmarks (Section 3.3.2) suggest a 1 GFLOP/core minimum processing capability. A multi-core desktop-style processor, several LEON3's, or a Virtex-5 FPGA are possibilities. The actual complexity of the detection software is also a concern; however, unlike the S/C operating system, the mission does not rely on the detection software as a critical component, so new software could be uploaded at will.

3.4.1.2 Compression Algorithm

Even with event detection, sending back raw imaging data during events would require a prohibitive amount of bandwidth. The data must be compressed in some manner to fit within bandwidth restrictions. However, since the raw data have very low SNR, standard compression algorithms are inappropriate. The solution is to notice that for waves in the airglow layer, the speed of sound waves requires a relationship between the frequency (ω) of a wave component and the wave vector (k).

The processing algorithm provides us with measurements of the dominant k_x , k_y , and ω , as well as the associated uncertainties, as a function of time. These parameters define a partial cylinder in ω - k space, and only values within the determined surface would need to be transmitted back for reconstruction and analysis on Earth. Therefore, the optimal compression algorithm is one similar to wavelet compression. The compression ratio of the algorithm may be easily computed by taking the ratio of the volumes of the Fourier-transformed data cube and the area of the embedded surface multiplied by the thickness required to capture sufficient fidelity for the science analysis.

3.4.2 Instrument Pointing Knowledge

The VAMOS instrument requires pointing accuracy to a fraction of a pixel over the image frame time of 2.5 seconds. More difficult is pointing knowledge since a star tracker capable of performing to a fraction of a pixel at the instrument would be of similar complexity to the VAMOS instrument itself. The proposed solution is to use the VAMOS instrument to update the pointing by imaging the limb of Venus. The limb is bright enough to saturate the detector using slow readout,

but a fast readout frame taken between science frames would require only 13 milliseconds. Onboard software would be required to find the center of the arc of the limb in these pointing frames and report any pointing offsets to the S/C ACS. Although the altitude of the airglow layer varies on the order of 20 km, this variation is averaged over a tangent through the ionosphere at the limb. This, as well as using a significant portion of the total limb to find the center of the disk, mitigates these altitude variations.

3.4.3 Improving SNR

The ability of VAMOS to detect weaker seismic activity is limited by the SNR of the signal, and the SNR is largely driven by shot noise from background airglow. The only way to improve the shot noise per unit time is to increase the single strength, or equivalently, the f-ratio of the optics. The f-ratio may easily be increased without significant degradation to the image quality, but at the cost of increased mass and volume. A design achieving f/3 is shown in Figure 3-8. However, the increase in input may be offset by losses at the narrow-band filters due to the increased angles of incidence. Performing a trade between the f-ratio of the loss at the narrow-band filters requires specific designs for the filters, which was beyond the scope of the current study.

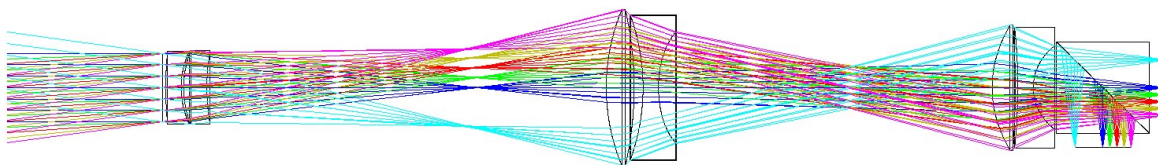


Figure 3-8. An f/3 design with equivalent performance to the f/4 design. The entrance aperture is 45 mm, while the FOV, EFL, and total track are identical.

3.4.4 Alternative Detector Technology

Many mid-wavelength infrared (MWIR) imaging space mission proposals use the Teledyne HgCdTe H2RG + SIDECAR detector technology because of the James Webb Space Telescope (JWST) heritage. For low to moderate SNR, this technology has no commercial competitor technology that works in the temperature ranges achievable by passive, radiative cooling. However, JPL has recently developed HOT-BIRD¹⁸, a detector technology based on the III-V semiconductor type-II superlattices. For MWIR wavelength ranges and detector temperatures near 80 K, the H2RG 5- μ m technology and HOT-BIRD detectors with similar cutoff wavelengths have very similar dark currents.

Teledyne technology is expensive and difficult to manufacture. An H2RG costs about \$1M and the SIDECAR firmware is typically another \$1M. Teledyne does, however, have high heritage (OCO-2, JWST, others).

On the other hand, InSb is much easier to manufacture and thus dominates the military market, even though standard InSb requires a much lower operating temperature. The HOT-BIRD technology, similarly to HgCdTe, may be tuned to a range of cutoff wavelengths, but with less difficulty than Teledyne has with developing new cutoff wavelength detectors with HgCdTe. The HOT-BIRD technology would require effort to be brought up to TRL-6 for flight.

4. MISSION CONCEPT DESCRIPTION

The unique observation strategy for VAMOS's infrared camera instrument dictates several atypical features of VAMOS's notional orbit, which place unique and driving requirements on the flight system design. An earlier version of the implementation with more details can be found in Didion *et al*¹⁹.

4.1 Mission Requirements

The baseline observation strategy places key requirements on the nominal orbit for the VAMOS orbiter at Venus and the associated flight system, detailed in Table 4-1. The orbit itself is notable for atypical features such as the combination of high orbital altitude with low eccentricity (circular) in order to perform persistent observations of the entire Venusian disk at all times. Insertion into this orbit favors a flight system equipped with SEP and penalizes a classical chemical propellant system.

Table 4-1. High-level mission requirements for the VAMOS mission concept and flight system.

Venusian Orbital Parameters	45k km radius, circular, near-equatorial
Science Mission Duration	1 Venus year
Science Duty Cycle	~ 100%
Launch Mass	< 180 kg
Stowed Volume Envelope	61 cm × 71 cm × 96 cm
Redundancy	Single-string
NASA Risk Class	D
Planetary Protection	None
Decommissioning	None

4.2 Mission Concept Description

The primary objective of the VAMOS mission design is to place the infrared imager into a 45,000 km radius circular, near-equatorial orbit while remaining within the launch vehicle performance of the ESPA-class secondary launch adapters. A circular orbit was selected as it maximized the observing time. A highly elliptical orbit would only be able to make observations near apoapsis and the resulting loss of observing time unacceptably reduces the likelihood of observing an entire Venus quake. The altitude was selected as the mass-optimal altitude. A higher altitude would require a larger telescope for the instrument, while a lower altitude would require greater propellant mass to spiral down, as shown in Figure 4-1.

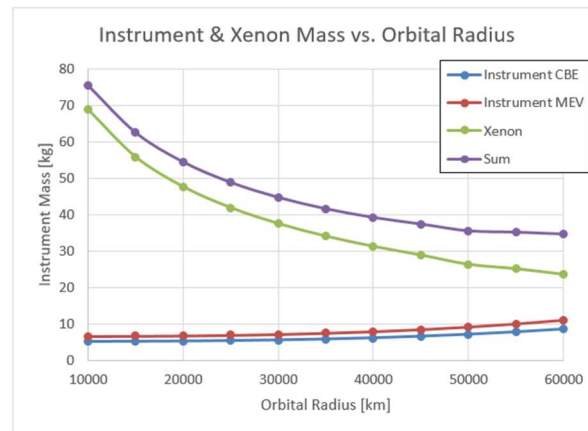


Figure 4-1. The mass trends of xenon load, telescope size, and the sum as a function of orbital radius, showing a favorable point design around 45,000–50,000 km.

VAMOS uses a solar electric propulsion (SEP) system as a co-manifest with a primary payload delivered into a geosynchronous transfer orbit (GTO). A sequence of short maneuvers and lunar flybys is then undertaken to escape the Earth-Moon system on the desired hyperbolic departure. A 30–51 month interplanetary cruise (spanning trajectory types of various number of revolutions) consisting of deep space SEP thrust arcs and a combination of Earth and Venus flybys ends in a distant rendezvous with Venus. The final 45,000 km circular orbit is then achieved by spiraling down. This cruise-and-spiral architecture was twice successfully executed by the Dawn spacecraft at Vesta and Ceres.

A SEP architecture was selected over a high-thrust chemical option as it provided the maximum opportunities for a co-manifest and remained within the 300 kg maximum capability of the ESPA Grande launch adapter. No option was found that would be capable of achieving the required science orbit within the 180 kg ESPA allocation. An extremely eccentric and polar orbit, with apoapsis around 360,000 km, is possible within that allocation, but the science objectives could not be met from such an elliptical orbit.

4.2.1 Trajectory Design

The trajectory design for any mission without a dedicated launch vehicle requires the maximum flexibility in terms of initial conditions. For this reason, VAMOS has selected a baseline mission enabled by solar electric propulsion.

4.2.1.1 Earth–Moon System Escape

One of the most likely rideshare options is to launch with a commercial geostationary satellite to a GTO. This rideshare option results in a substantially reduced launch cost, but there is no control of the launch conditions and the spacecraft is not nominally on an escape trajectory from Earth. Instead, an indirect escape must be used. First, the upper stage of the launch vehicle must boost the VAMOS spacecraft to an apogee well beyond the Moon. This requires 680–745 m/s if performed at perigee. In the absence of the launch-vehicle supplied apogee boost, the SEP ΔV and flight times become excessive and the mission is likely not feasible.

After the apogee boost, a series of maneuvers is performed to target a sequence of lunar flybys, illustrated in Figure 4-2, producing the desired escape conditions. The GTO node can be distant from the Moon's orbital node, therefore it is generally necessary to perform a plane change at apogee to set up a lunar flyby. An analysis was performed to bound the range of required SEP ΔV for a spacecraft departing the Earth-Moon system from a GTO. Literature²⁰ shows that two lunar flybys can produce a hyperbolic escape energy $C3$ of about $2 \text{ km}^2/\text{s}^2$. To be conservative and increase the range of feasible escape sequences, the escape $C3$ is constrained to be less than $1 \text{ km}^2/\text{s}^2$.

If a rideshare is available on a mission to the Moon (e.g., an Exploration Mission SLS launch) or to the Earth–Sun Lagrange points (e.g., the proposed NEOCam mission or other deep space telescopes), this same architecture can be implemented with far less SEP ΔV and shorter flight times. If deployed into the GEO ring (or just above it), and escape would also be possible by spiraling out and targeting the lunar flyby. This would require more xenon but would be feasible.

4.2.1.2 Interplanetary Cruise

As illustrated in Figure 4-3, after the spacecraft departs the Earth-Moon system, it enters an Earth trailing orbit. A pair of SEP thrust arcs centered on perihelion and aphelion increase the Earth-relative velocity sufficient to enable a nearly ballistic Earth–Venus transfer. If VAMOS were to obtain a dedicated launch or a rideshare with a Venus-destined spacecraft, this Earth Gravity Assist (EGA) would become the launch and several 10's of kg of xenon propellant would be saved.

Following the EGA, a Venus Gravity Assist (VGA) is used to simultaneously lower aphelion to closer to that of Venus and match the heliocentric inclination to that of Venus. This orbit, then, is a Venus trailing orbit. After VGA, a series of thrust arcs raises perihelion and lowers aphelion over the course of slightly more than a Venus year until a distant rendezvous is achieved. Adding a full additional Venus year to this leg of the journey saves only 1 kg of xenon, as the thrust arcs can be shorter and thus more optimally located. Operations costs of this longer trajectory and the associated lifetime risks would not be worth such a small savings.

4.2.1.3 Science Orbit

The 45,000 km science orbit was selected as a balance point for the mass of xenon required to achieve this orbit and the mass of the optics within the instrument to achieve the required resolution. A higher orbit would require less xenon, but heavier optics. At this altitude, the orbit period is 29.2 hours, and the worst-case eclipse duration is 75 minutes. The spacecraft batteries are sized to permit continual science operations during this worst-case eclipse. The orbit inclination is 10° so as to get as close to fully-lit and fully-dark disks as possible while limiting eclipses to discrete seasons.

Once the 45,000 km circular orbit near-equatorial orbit is achieved, no maintenance maneuvers are required. The orbit is high enough that the atmosphere and non-sphericity of Venus are non-factors, and the circular orbit altitude is essentially immune to solar perturbations. The Sun does induce an inclination oscillation, but the VAMOS observations do not depend on a particular inclination and so these effects can be left uncontrolled.

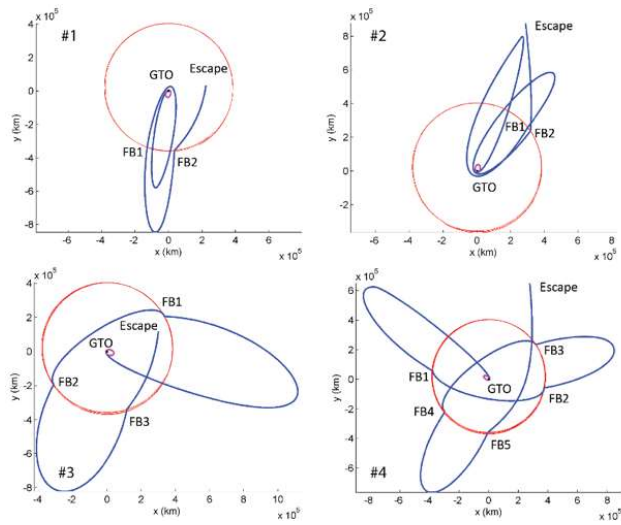


Figure 4-2. Four lunar flyby sequences were examined to size the ΔV required to escape the Earth–Moon system: (1) One outbound and one inbound flyby. (2) Two outbound flybys. (3) One inbound flyby to setup a backflip then an outbound and an inbound flyby. (4) Five flybys, including two backflips.

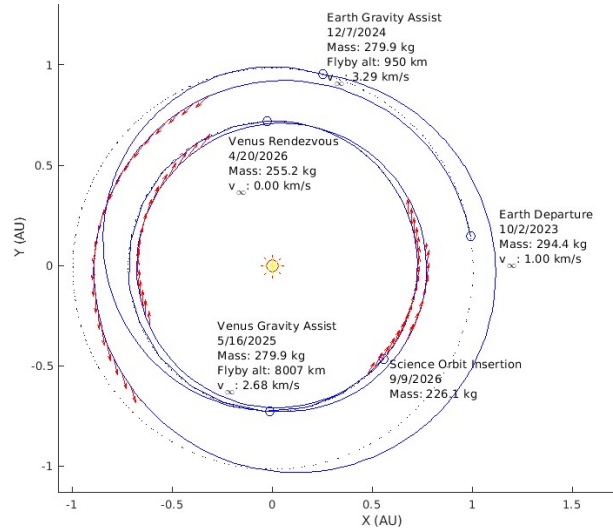


Figure 4-3. A worst-case escape followed by a 31 month cruise and a 5-month spiral down achieves the science orbit with 74 kg of xenon.

End-of-mission disposal is achieved by simply deactivating the spacecraft in its orbit, as there is no planetary protection need nor cost-effective means for decommissioning via de-orbit. The additional ΔV capability necessary to de-orbit would be prohibitively expensive and massive.

4.2.2 Flight System Capabilities

The VAMOS flight system is designed to best suit the needs of the science-observing scenario and mission design, while making use of commercial SmallSat hardware and NASA Class D procedures to optimize mass and cost.

4.2.2.1 Spacecraft Parameters

The VAMOS spacecraft was designed primarily during a JPL Team X design study, using institutional mass and cost models as if the spacecraft were to be built by JPL or a subcontractor according to Class D standards and a single-string redundancy approach.

Configuration of the spacecraft is driven primarily by key features such as the large solar arrays and instrument radiators and drives the science operations (see Section 4.2.6).

4.2.2.1.1 Power Subsystem

The VAMOS baseline mission design (Section 4.2.1.2) has the spacecraft cruise to Venus under low-thrust SEP (hardware described in Section 4.2.3.1.6), which requires the spacecraft to gather large amounts of solar power during cruise. This design improves as the spacecraft approaches Venus, closer to the Sun, and leaves the spacecraft with a wealth of excess power generation during the science acquisition phase in Venusian orbit. Unused power generation capability can be eliminated through solar array off-pointing.

The high circular orbit at Venus means eclipses are longer, but further apart, and can be sequestered to “eclipse seasons” by inclining the final orbit at the expense of minor impacts to the instrument and thermal subsystems.

4.2.2.1.2 Command and Data Subsystem

Real-time processing of the science data to detect phenomena and collect products for downlink only when phenomenon is confirmed was found to be a largely driving requirement for the VAMOS Command and Data Subsystem (CDS, C&DH). The processing rate required to handle real-time science observations (~1 GFLOPS, Section 3) is beyond the capabilities of all commercial SmallSat CDS hardware, and so the baseline design has a dual-RAD750 architecture. In this

architecture, a RAD750 and its standard set of complementary hardware handle all spacecraft computer functions while a separate RAD750 and specialized custom card handle image processing. This architecture can meet the computing needs of the VAMOS science observing scenario but costs and weighs a significant amount.

A single event (predicted at 4/week) can produce approximately 7 GB of raw data, which would need to be processed down to 10 MB for downlink. On demand, a raw frame, unprocessed by the event detection algorithms but compressed for downlink (~1.5 MB) can be commanded for downlink.

4.2.2.1.3 Telecommunications Subsystem

The baseline telecommunications strategy is to downlink only spacecraft health/status telemetry and key raw images in between event detections, rather than attempt to stream the prohibitively large amount of data to Earth for ground processing. As discussed in the CDS Section 4.2.2.1.2, instrument data is to be processed in real time to detect seismic event phenomena. When an event is confirmed, the resulting data is packaged for downlink.

The VAMOS telecommunications system is sized to return data to 34 m DSN antennas at rate of 650 bps from 1.7 AU (maximum Earth–Venus range) and 14 kbps from 0.3 AU (minimum); the uplink rate is 12 bps. During downlink, science observations are paused.

VAMOS' telecom hardware consists of an IRIS CubeSat radio operating on X-band with no SSPA and a 25 W X-band TWTA. The spacecraft has one X-band MGA and one X band LGA. Use of the IRIS assumes that the IRIS has been fully qualified by that point in time, this is a possible development risk.

4.2.2.1.4 Spacecraft Structure

The VAMOS flight system was designed to fit within the evolved expendable launch vehicle (EELV) secondary payload adapter (ESPA) volume allowance of 61 cm × 71 cm × 96 cm and was given the same rectangular prism shape as this envelope. It was found through the Team X study that the flight system would fit with only minor interferences (64 cm × 72 cm × 91 cm), very likely resolvable in future study.

4.2.2.1.5 Thermal Control Subsystem

The baseline instrument does not require an active cryo-cooling system and is designed to dissipate its excess heat through dedicated multi-stage radiators rather than passing it to the spacecraft (Figure 4-4 and Section 3.1.2). Operationally, the science orbit planning will have to take into account these radiators and avoid pointing them near the Sun while the spacecraft remains nadir-pointed.

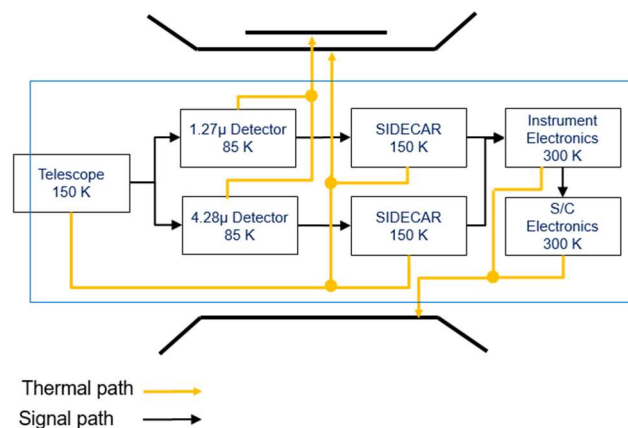


Figure 4-4. The VAMOS instrument requires dedicated 2-stage radiators to sufficiently cool its electronics and detectors. These radiators are simpler than active cryo-cooling but would be sensitive to solar impingement.

The hottest case in the nominal mission is during the spiral-down at Venus, where the spacecraft is operating the SEP system while at its closest distance to the Sun. The coldest case is during eclipse, where the spacecraft is occulted from the Sun by Venus, but still at high altitude from Venus where it does not receive substantial planetary infrared radiation.

4.2.2.1.6 Propulsion Subsystem

The JPL Magnetically Shielded Hall Thruster (MaSMi) electric propulsion system was chosen as the baseline engine. The MaSMi is a TRL 4 JPL-developed thruster which features magnetic shielding to improve life span by greatly increasing the total xenon throughput capability. It is expected that the MaSMi thruster would be capable of processing considerably more propellant due to its magnetic shielding technology. Both thrusters need further technology development prior to flight use; either could be ready for flight with approximately 2–3 years of development.

The MaSMi system (Figure 4-5) is designed to operate at a nominal 600 W, but the PPU architecture will provide greater throttling capability (3–6 points) from ~200 W to > 800 W with peak specific impulses of > 1,600 s expected over the lower range. Either system would require array power generation levels around 1 kW.

The system uses a heritage xenon feed system from the Falconsat-5 mission. The xenon propellant would be stored in a commercially available ATK PN 80412-1 composite propellant tank of dimensions 0.325-m diameter and 0.699-m length, capable of storing approximately 70–80 kg of xenon, or a PN 80458-201 for approximately 100 kg.

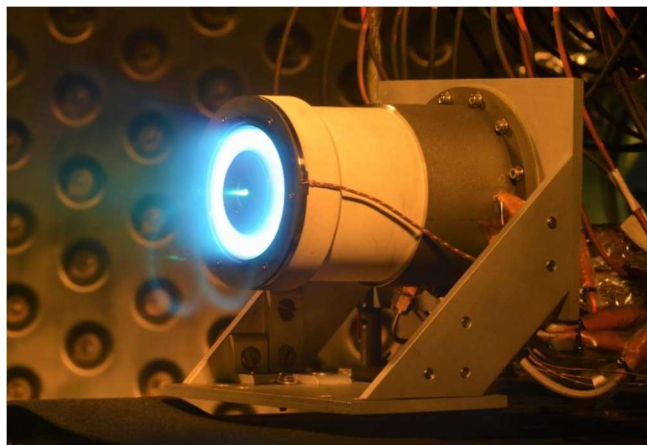


Figure 4-5. The MaSMi thruster is a JPL-developed magnetically shielded, center-cathode Hall thruster, shown operating at 500 W discharge power.

4.2.2.1.7 Attitude Determination and Control Subsystem

Due to the large deployable solar arrays and relatively strict pointing requirements of the optical instrument (see Section 3), it was found that small all-in-one ADCS systems are incapable of controlling the baseline VAMOS flight system. The ADCS hardware chosen instead includes four Surrey sun sensors, 2 Terma HE-SAS star trackers, one Litton IMU, and three Rockwell 4 Nms orthogonally-mounted reaction wheels.

The reaction control system (RCS) is a blow-down hydrazine monopropellant system, used for momentum control, as Venus' lack of magnetic field precludes use of magnetic torque rods. The system consists of 8 Aerojet MR-103M thrusters capable of 1 N, and a single ATK 80222-1 titanium diaphragm tank, spherical, with diameter 0.239 m, with approximately 3.7 kg of hydrazine propellant and residuals.

4.3 Performance and Design Margins

The VAMOS SEP baseline fits within the ESPA Grande mass allocation with proper contingencies and margins. Figure 4-6 shows a high-level pie chart of the MEV dry mass breakdown.

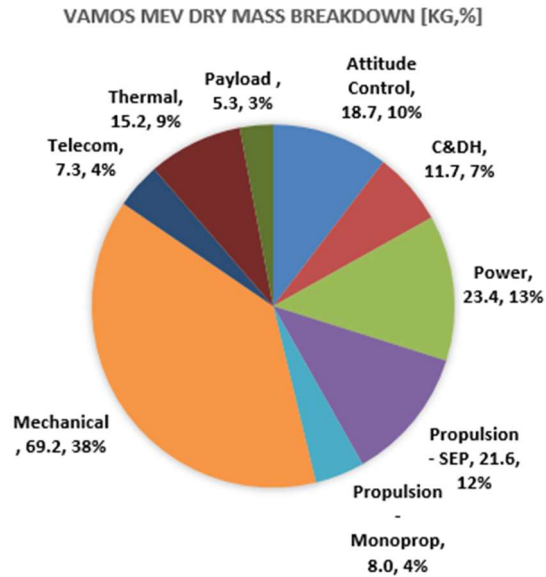


Figure 4-6. The baseline VAMOS SEP spacecraft design is 180 kg dry MEV, divided as shown here. Additionally, the spacecraft requires 70–78 kg of xenon propellant and approximately 4 kg of hydrazine RCS propellant.

ACKNOWLEDGEMENTS

This work was conducted at the NASA Jet Propulsion Laboratory, a division of California Institute of Technology, and was partially funded by a NASA Planetary Science Deep Space SmallSat Study, NNH16ZDA001N-PSDS3. Some material in this paper has been previously presented^{19,21,22}. The information provided about the VAMOS mission concept is pre-decisional and is provided for planning and discussion purposes only.

REFERENCES

- [1] Ducic, V., Artru, J. and Lognonné, P., “Ionospheric remote sensing of the Denali Earthquake Rayleigh surface waves,” *Geophys. Res. Lett.* 30(18), 1951, doi: 10.1029/2003GL017812 (2003).
- [2] Artru, J., Farges, T., Lognonné, P., “Acoustic waves generated from seismic surface waves: propagation properties determined from Doppler sounding observation and normal-modes modeling,” *Geophys. Jour. Int.* 158, 1067-1077, doi:10.1111/j.1365-246X.2004.02377.x (2004).
- [3] Garcia, R., Lognonné, P. and Bonnin, X., “Detecting atmospheric perturbations produced by Venus quakes,” *Geophys. Res. Lett.* 32, L16205, doi: 10.1029/2005GL023558 (2005).
- [4] Calais, E. and Minster, J. B., “GPS detection of ionospheric perturbations following the January 17, 1994, Northridge earthquake,” *Geophysical Research Letters* 22, 1045–1048 (1995).
- [5] Kelley, M., Livingston, R. and McCready, M., “Large amplitude thermospheric oscillations induced by earthquakes,” *Geophysical Research Letters* 12, 577–580 (1985).
- [6] Lognonné, P. and Johnson, C., “Planetary Seismology,” [Treatise in Geophysics, 10, Planets and Moons], editor G. Schubert, chapter 4, 69–122, Elsevier, doi:10.1016/B978-044452748-6.00154-1 (2007).
- [7] Lognonné, P. and Johnson, C. L., “10.03 - Planetary Seismology,” [Treatise on Geophysics (Second Edition)], editor Gerald Schubert, Elsevier, Oxford, 65–120, ISBN 9780444538031, doi:10.1016/B978-0-444-53802-4.00167-6 (2015).
- [8] Lognonné, P., Karakostas, F., Rolland, L., Nishikawa, Y., “Modeling of atmospheric-coupled Rayleigh waves on planets with atmosphere: From Earth observation to Mars and Venus perspectives,” *Journal of the Acoustical Society of America* 140, 1447–1468, doi:10.1121/1.4960788 (2016).
- [9] Grawe, M. A., Makela, J., “Observation of tsunami-generated ionospheric signatures over Hawaii caused by the 16 September 2015 Illapel Earthquake,” *J. Geophys. Res.* 122, 1128–1136, doi:10.1002/2016JA023228 (2017).

- [10] Grawe, M. A. and Makela, J. J., "The ionospheric responses to the 2011 Tohoku, 2012 Haida Gwaii, and 2010 Chile tsunamis: Effects of tsunami orientation and observation geometry," *Earth and Space Science* 2, 472–483, doi:10.1002/2015EA000132 (2015).
- [11] Garcia, R. F., Drossart, P., Piccioni, G., López-Valverde, M., Occhipinti, G., "Gravity waves in the upper atmosphere of Venus revealed by CO₂ nonlocal thermodynamic equilibrium emissions," *J. Geophys. Res.* 114, CiteID E00B32 (2009).
- [12] López-Valverde, M. A., Drossart, P., Carlson, R., Mehlman, R., Roos-Serote, M., "Non-LTE infrared observations at Venus: From NIMS/Galileo to VIRTIS/Venus Express," *Planet. Space Sci.* 55, 1757, doi:10.1016/j.pss.2007.01.008 (2007).
- [13] Peralta, J., López-Valverde, M. A., Gilli, G. and Piccialli, A., "Dayside temperatures in the Venus upper atmosphere from Venus Express/VIRTIS nadir measurements at 4.3 μm ," *A&A* 585, A53, doi:10.1051/0004-6361/201527191 (2016).
- [14] López-Valverde, M., López-Puertas, M., Funke, B., Gilli, G., Garcia-Comas, M., Drossart, P., Picconi, G., Formisano, V., "Modeling the atmospheric limb emission of CO₂ at 4.3 mm in the terrestrial planets," *Planet. Space Sci.*, doi:10.1016/j.pss.2010.02.001 (2010).
- [15] Teledyne, "Teledyne imaging sensors H2RG™ visible & infrared focal plane array," September 2017, <http://www.teledyne-si.com/products/Documents/H2RG%20Brochure%20-%20September%202017.pdf> (2018).
- [16] Helbert, J., Wendler, D., Walter, I., Widemann, T., Marcq, E., Maturilli, A., Ferrari, S., D'Amore, M., Mueller, N., Dyar, M. D., Smrekar, S., "The Venus Emissivity Mapper (VEM) concept," 47th Lunar and Planetary Science Conference (2016).
- [17] Brecht, A., S. W. Bougher, J.-C. Gerard, L. Soret, Atomic Oxygen Distributions in the Venus Thermosphere: Comparisons Between Venus Express Observations and Global Model Simulations, *Icarus*, 117, 759-766, doi:10.1016/j.icarus.2011.06.033, (2012).
- [18] Ting, D., Hill, C., Soibel, A., Bandara, S., Gunapala, S., "High-Operating-Temperature Barrier Infrared Detector With Tailorable Cutoff Wavelength," NASA Tech Briefs, NPO-46477, p. 16, February, (2011).
- [19] Didion, A., A. Komjathy, B. Sutin, Nakazono, B., Karp, A., Wallace, M., Lantoine, G., Krishnamoorthy, S., Rud, M., Cutts, J., Makela, J., Grawe, M., Lognonné, P., Kenda, B., Drilleau, M., Helbert, J., "Remote Sensing of Venusian Seismic Activity with a Small Spacecraft, the VAMOS Mission Concept." Accepted in IEEE Aerospace Proceedings, Big Sky, MT, March 3-10, (2017).
- [20] McElrath, T., Lantoine, G., Landau, D., Grebow, D., Strange, N., Wilson, R., Sims, J., "Using gravity assists in the Earth-Moon system as a gateway to the solar system," Paper GLEX 2012.05.5.2x12358 (2012).
- [21] Kenda, B., Lognonné, P., Komjathy, A., Banerdt, B., Cutts, J., Sutin, B., Didion, A., Jackson, J., "Modeling airglow disturbances induced by quakes on Venus: Perspectives for future observations," *Proc. Lunar and Planetary Science Conference* 49, 2393 (2018).
- [22] Komjathy, A., Didion, A., Sutin, B., Nakazono, B., Karp, A., Wallace, M., Lantoine, G., Krishnamoorthy, S., Rud, M., Cutts, J., Makela, J., Grawe, M., Lognonné, P., Kenda, B., Drilleau, M., Helbert, J., Remote Sensing of Seismic Activity on Venus Using a Small Spacecraft: Initial Modeling Results, Presented at the Lunar and Planetary Science Conference, The Woodlands, Texas, March 19-23, (2018). <https://www.hou.usra.edu/meetings/lpsc2018/pdf/1731.pdf>